ACI MATERIALS JOURNAL TECHNICAL PAPER

Title No. 120-M24

Evaluation of Sulfate Resistance of One-Part Alkali-Activated Materials Prepared by Mechanochemistry

by Wenda Wu, Shilong Ma, Yuanda Wang, Xuefang Wang, Liwei Xu, and Shichang Ye

In this paper, the resistance of mechanically prepared one-part alkali-activated materials to external sulfuric acid attack was investigated by simulating realistic erosion environments in terms of sulfate type, concentration, and erosion mode. The macroscopic properties of the specimens were measured at different ages. Microscopic analyses were performed by Fourier-transform infrared spectroscopy (FTIR), X-ray diffraction (XRD), mercury intrusion porosimetry (MIP), and other techniques to obtain the effect of different erosion environments on the mechanical-force chemically prepared one-part alkali-activated materials against sulfate erosion. The study shows that the mechanical properties of the specimens showed a trend of increasing and then decreasing with the extension of erosion time. Compared with Na_2SO_4 erosion, the erosion damage was greatest when the sulfate containing Mg^{2+} was eroded in a wetting-and-drying cycle; the erosion products of Na_2SO_4 solution coexist in the form of calcite and gypsum, while the erosion products of $MgSO_4$ solution mainly consist of gypsum.

Keywords: mechanochemistry; one-part alkali-activated materials; sulfate attack.

INTRODUCTION

One-part alkali-excited cementitious material refers to an inorganic nonmetallic material with cementitious activity that is prepared by mixing a solid alkaline exciter with a mineral material with volcanic ash activity according to a certain process.[1,2] This one-part alkali-initiated gelling material is similar to ordinary portland cement (OPC) and can be used by adding water. Alkali-excited gelling materials have attracted great attention from academic authors worldwide for their excellent performance. In the 1940s, Purdon[3] experimentally prepared a geopolymer mixture by simply mixing slag with solid sodium hydroxide and successfully prepared a gelling mixture. At the beginning of the twenty-first century, Duxson and Provis[4] outlined various potential methods for tuning the precursor chemistry and particle behavior of geopolymers and proposed a one-part geopolymer that exceeded the potential of conventional two-part (solid plus alkaline-activator solution) hybrid designs. Peng et al.[5] prepared a one-part geopolymer with excellent compressive strength by a process of calcined bentonite and the addition of solid alkali, which exceeded the compressive strength of a two-part geopolymer with the same ratio and achieved a higher softening factor of 0.93. Additionally, in terms of environmental protection and economy, the raw material sources of alkali-inspired cementitious materials are mostly fly ash, slag, and other industrial waste. These substances have a low cost, simple preparation process, less energy consumption, and only 26 to 45% of the carbon emissions of OPC and are therefore recognized as green cementitious materials.[6-8]

In recent years, researchers have found that the treatment of alkali-excited precursors using mechanical-force chemistry enables the effective release of volcanic ash activity from the precursors, leading to the improvement of various properties, such as the efficiency of curing toxic heavy metal ions and thermal stabilities.[9] The study by Temuujin et al.[10] showed that mechanical-force chemistry changed the physical properties of fly ash and directly affected the volcanic ash reaction of alkali-excited materials. Also, the 28-day compressive strength of alkali-excited fly ash net slurry specimens subjected to mechanical-force chemistry increased by 80%. Kumar et al.[11] proposed that mechanical activation can enhance the reactivity of alkali-excited slag cement net slurry, enabling it to react with water directly and harden, and suggested that the volcanic ash reactivity of slag cement is related to its specific surface area. Zhao et al.[12] found that mechanical activation resulted in optimized particle-size distribution, superior pore structure of alkali-excited fly ash mortar, and reduced aggregation of SiO_4 tetrahedra and AlO_4 tetrahedra in the gel. These studies show that the preparation of single-part alkali-excited gelling materials using mechanical-force chemistry has been recognized by a wide range of researchers and has become a research hot spot in the field of new green building materials.

The issue of durability of concrete has been a decisive factor in the service life of buildings, and the erosion damage of concrete by sulfate is one of the reasons for the serious reduction of durability.[13,14] Previous studies[15-17] have shown that sulfate erosion will cause the expansion of the cementitious material and produce cracks and peeling, which has a great negative impact on its strength and durability. Global maintenance and repair costs due to corrosion alone exceed $150 billion annually.[18,19] The environments in which buildings are located have contributed to diversity in sulfate erosion.[20-22] For example, inland saline areas contain high concentrations of mirabilite ($Na_2SO_4 \cdot 10H_2O$), and sulfate erosion is dominated by salt (Na^+). In contrast, the sulfate ($MgSO_4$) in seawater mainly causes building erosion in coastal areas. In addition, some buildings are partially submerged in seawater for a long period, as well

ACI Materials Journal, V. 120, No. 2, March 2023.

MS No. M-2022-108.R5, doi: 10.14359/51738491, received October 8, 2022, and reviewed under Institute publication policies.

Table 1—Chemical composition of materials, wt. %

Mineral composition	SiO_2	Al_2O_3	Fe_2O_3	MgO	CaO	Na_2O	K_2O	MnO	TiO_2	Loss
Fly ash	45.9	34	5	0.8	6.9	0.2	0.9	0.1	1.7	4.5
Slag	28.7	14	0.4	9.9	41.2	0.5	0.4	0.3	1.4	3.2

as wetting-and-drying circulation areas in splash zones and tidal zones. Therefore, it is necessary to test the sulfate resistance of single-component alkali-initiated gelling materials before they are widely used in practical engineering.

To more closely simulate the authentic environments in which the building is located, Mg^{2+} and Na^{+}, which are more widely distributed, were selected as the metal cations of sulfate erosion solution in this paper. Realistic sulfate erosion environments were simulated by adjusting sulfate solution concentrations (that is, 5 and 10%) and erosion methods (that is, wetting-and-drying cycles and full immersion). At the same time, the sulfate resistance performance was compared with that of OPC to make a comprehensive evaluation of the sulfate resistance of single-part alkali-excited materials prepared by mechanical-force chemistry.

RESEARCH SIGNIFICANCE

The preparation process of one-part alkali-activated materials by mechanical-force ball milling is simple, does not require a high-temperature calcination process, consumes less energy, and has only one-third of the carbon emissions of OPC, which is recognized as a green cementitious material. The investigation of the sulfuric acid resistance of the single-component alkali-initiated material prepared by a mechanical-force ball mill is important preparation for the promotion of the material in practical engineering applications. It is also an effective measure to replace the use of portland cement (PC) and reduce carbon emissions, thereby exhibiting significant research significance.

MATERIALS AND EXPERIMENTS

Raw materials

Material preparation—For this study, fly ash and slag were purchased from the same Chinese mining company. They were used as alkali-excited precursors, where the average particle size of raw fly ash was approximately 63.72 μm, the water requirement was 80%, the 45 μm sieve margin was 15.15%, the average particle size of raw mineral powder was approximately 15.7 μm, and the 28-day activity index reached 98%. Table 1 and Fig. 1 display the chemical composition and crystal composition, respectively. According to Fig. 1, the main crystalline phases in fly ash are mullite and quartz, which also contain amorphous glass phases. Slag is mainly composed of an amorphous glass phase and calcium oxide, and a small amount of calcite.

For the experimental control group, P.O42.5R OPC produced by a cement factory in China was purchased, with a density of 3150 kg/m^3 and a specific surface area of 352 m^2/kg. The cement met the requirements of EN 197-1:2011. Table 2 presents the chemical composition of the cement.

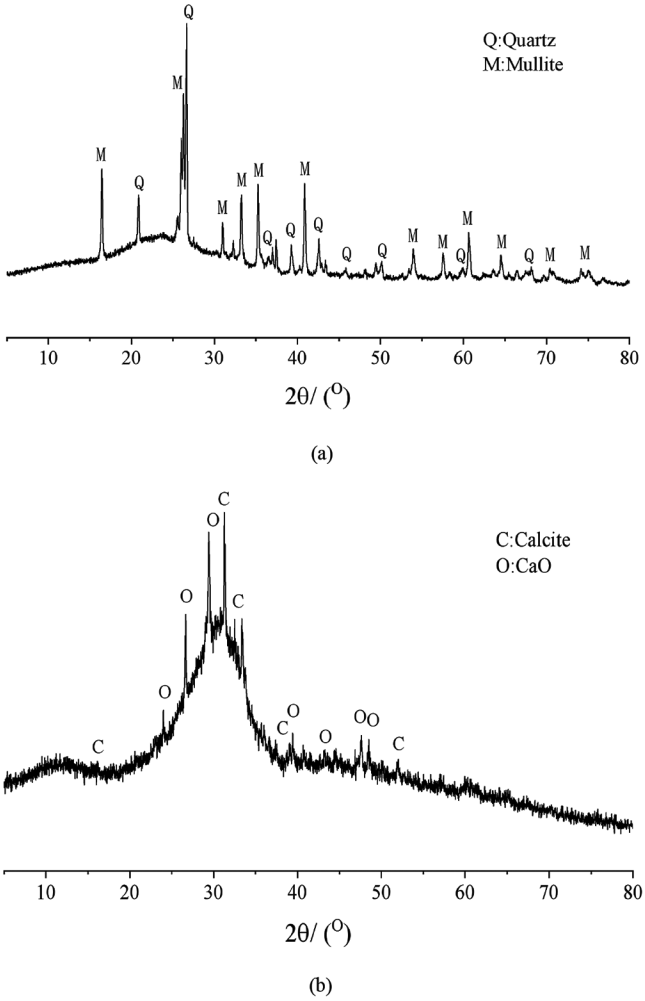

Fig. 1—(a) XRD spectra of original fly ash; and (b) XRD spectra of original slag.

Furthermore, in this study, analytical pure barium chloride was used as a retarder and International Organization for Standardization (ISO) standard sand as mixed sand.

Preparation of alkali-activated materials and sulfate solution—The preparation method of one-part alkali-activated material prepared by mechanochemistry is as follows: first, heat the slag powder and fly ash in an oven at 100 ± 5°C for 2 hours to remove the moisture. Remove the slag powder and fly ash and cool to room temperature. Place the slag powder, fly ash, and solid activator together into a ball mill tank. Use the ball mill to mill the mixture for 30 minutes. Finally, store the milled powder in a sealed bag to inhibit moisture and carbonization. The size of the steel balls in the ball mill was 30, 20, and 10 mm in diameter, the mass ratio was 1:1:1, and the packing density of the steel balls was 4640 kg/m^3. In this experiment, anhydrous NaOH and Na_2SiO_3 were used as alkali activators, where the purity of NaOH was over 96% and the purity of Na_2SiO_3 with SiO_2:Na_2O of 1.4 was over 99%.

Table 2—Chemical compositions of cement, wt. %

Mineral composition	SiO_2	Al_2O_3	CaO	Fe_2O_3	SO_3	MgO	f-CaO	Other	Ignition loss
Value	21.7	4.4	62.5	3.3	2.9	2.1	0.6	0.9	1.6

Table 3—Specimen mixture proportions

Material	Fly ash, %	Slag, %	Portland cement, %	*w/c*	Sand-glue ratio	Alkali-excitation agent, %	Retarder, %
Alkali-activated materials	75	25	—	0.4	0.5	4	1
OPC	—	—	100	0.4	0.5	—	—

Table 4—Test design scheme

Numbering	Sulfate species	Sulfate concentration, %	Erosion mode
M5F	$MgSO_4$	5	Full immersion
M10F	$MgSO_4$	10	Full immersion
N5F	Na_2SO_4	5	Full immersion
N10F	Na_2SO_4	10	Full immersion
M5DW	$MgSO_4$	5	Wetting-and-drying cycles
N5DW	Na_2SO_4	5	Wetting-and-drying cycles
S-M5F	$MgSO_4$	5	Full immersion
O-M5F	$MgSO_4$	5	Full immersion

Note: M is $MgSO_4$; N is Na_2SO_4; F is full immersion; DW is wetting-and-drying cycles; S is simple mixing; O is OPC; numbers denote sulfate solution concentration. (For example, O-M5F denotes full-immersion erosion of specimen prepared with OPC under 5% $MgSO_4$.)

The sulfates used in this experiment were analytically pure anhydrous Na_2SO_4 and anhydrous $MgSO_4$, and the purity of both sulfates exceeded 99%. The configuration steps are as follows: First, weigh an appropriate amount of solid sulfate and deionized water, as required. Then, prepare the sulfate attack solution, according to the configuration standard of the sulfate solution.

Experimental scheme and specimen preparation

Experimental scheme—Table 3 presents the mixture proportions selected in this study (the percentages in the table are quality percentages).

To facilitate accuracy, the test scheme adopted the single control variable method to create erosion tests of various influencing factors, as Table 4 illustrates. At the same time, two control groups were established, which were simple mixing mortar (simple mixing of precursor and alkali activator without mechanical grinding) and OPC mortar specimens. Then, the authors compared the resistance to sulfate attack of the various one-part alkali-activated slag-fly ash mortar specimens prepared by mechanochemistry.

After 28 days of standard curing, the specimens were placed in various pieces of equipment according to the different erosion methods. The full-immersion specimens were placed in a constant temperature and humidity curing box, as Fig. 2(a) illustrates. For the wetting-and-drying cycles, the samples were placed in a self-made automatic wetting-and-drying cycle device, shown in Fig. 2(b). The automatic wetting-and-drying cycle device was maintained at a constant temperature (20°C) and humidity (40%). The wetting-and-drying cycle mode is 16 hours of full immersion and 8 hours of drying, followed by a complete wetting-and-drying cycle for 24 hours. The sulfate erosion solutions were changed monthly during the experiment to reduce errors caused by changes in concentration. When the age of erosion reached 30, 60, and 90 days, the specimens were analyzed for appearance, compressive and flexural strengths, and microscopic variations. Ultimately, the mechanism of the effects of different erosion environments on the one-part alkali-activated materials prepared by mechanochemistry against sulfate erosion was obtained.

Specimen preparation—When the mortar specimen reaches the age of erosion (that is, 30, 60, and 90 days of erosion), the mortar sample from 0 to 5 mm from the surface of the specimen was removed by a cutting machine. The removed samples were crushed into pieces and placed in reagent bottles containing anhydrous ethanol to terminate the volcanic ash reaction. The instruments used for each microscopic test are as follows:

1. Fourier-transform infrared spectroscopy (FTIR): The instrument used in this study is a Fourier-transform infrared spectrometer produced in the United States. The wave number range of the instrument was set from 4000 to 400 cm^{-1} with a resolution of 12.5 px^{-1} and a wave number accuracy of 0.25 px^{-1}. The KBr compression method was used as follows: first, the oven was set to 120°C for drying the potassium bromide powder. Then, 1 mg of sample powder and 100 mg of potassium bromide powder were weighed with an accuracy of 0.1 mg. Subsequently, the mixed powder was ground in an agate mortar and a tablet pressing mechanism was used to make a disc without cracks and with a certain degree of translucency. Finally, the discs were put into the machine to start the test.

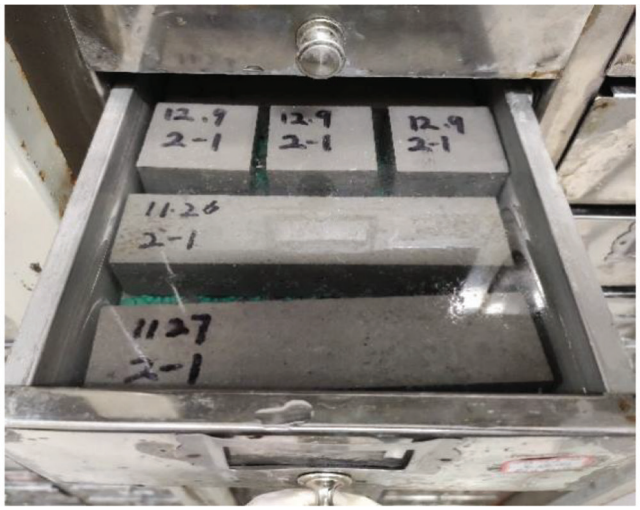

(a)

(b)

Fig. 2—(a) Full-immersion erosion in mortar specimen curing box; and (b) drying-and-wetting erosion of mortar specimens.

2. X-ray diffraction analysis (XRD): The instrument used in this study is an X-ray polycrystalline diffractometer. The 2θ angle range of the test instrument is –110 to 162 degrees, and the resolution full width at half maximum (FWHM) is 0.028 degrees. Before grinding, anhydrous ethanol was poured into the mortar to prevent carbonization of the mortar sample during the grinding process. After grinding, the paste-like samples were loaded into an aluminum box. The aluminum box was placed in a vacuum drying oven and baked at 50°C for 24 hours. The coarse particles in the dried powder were removed with a sieve disc of 0.08 mm aperture, and the sieved powder was put into a sealed bag.

3. Pore structure analysis (that is, mercury intrusion porosimetry [MIP]): The instrument used in this study is a mercury-pressure instrument. The aperture range of the instrument is 0.003 to 1080 μm. A 1.5 g sample was used for the test and was put into the expander and then vacuumed until $p <$ 6.67 Pa. The whole test must go through two stages of low pressure (1.03 to 25 psi) and high pressure (5 to 50,000 psi) to obtain two sets of data, respectively, after which these two sets of data are processed to obtain the analytical data of the sample pore structure.

RESULTS AND DISCUSSION

Effect of different erosion conditions on specimen strength

Figures 3 and 4 display the changes in compressive and flexural strength of the specimens under different erosion conditions. It includes changes in strength and strength loss rate, which is the loss rate of specimen strength at the next phase compared to the strength in the previous phase. It was found that the strength of the test specimens exhibits three phases with increasing erosion time. In the first stage from 0 to 30 days—namely, the growth stage—the strength of the specimens gradually increases with erosion time. In the second stage, which is the transition period at 30 to 60 days, specimen strength growth slows and stabilizes. Then, there is a transition from strength growth to loss. In the third stage, which is the declining stage between 60 to 90 days, the strength of the specimens gradually decreases with erosion.

During the initial growth phase in the first 30 days, the growth in strength of the specimens is mainly caused by two aspects. First, volcanic ash-active substances in the slag and fly ash lead to the hydration of alkali-excited materials. It can be hypothesized that silica-aluminous salts with volcanic ash activity and C-S-H undergo volcanic ash reactions to produce the denser $Ca(SiO_4)_2$,[23] and the accumulation of $Ca(SiO_4)_2$ fills the pores in the concrete. The other factor is the erosion of sulfate, which means that gypsum and ettringite form and accumulate in the micropore structure when the specimen is eroded by sulfate.[24,25] The accumulation of erosion products such as gypsum and ettringite causes expansion, which is beneficial to the strength of the specimen in the early stage of erosion. Figures 3 and 4 illustrate that the compressive strength loss rate of the N5DW specimen is the highest in the initial stage, reaching –19.1%. In contrast, the compressive strength loss rate of the corresponding $MgSO_4$ wetting-and-drying cycle erosion specimen M5DW is only –8.4%. The influence of the wetting-and-drying cycle erosion modes of two sulfates on the compressive strength of the specimens is greater than full-immersion erosion under the same conditions. Compared with sulfate concentration, the compressive strength and flexibility strength of the N5F specimens increases significantly under Na_2SO_4 erosion at low concentrations, and the loss rates are –12.2 and –4.9%, while the N10F specimens present losses of –3.0 and –2.2%. Conversely, the compressive and flexural strengths of the M10F specimens changed significantly under $MgSO_4$ erosion, with loss rates of –5.5% and –13.5%, respectively, while the loss rates of M5F specimens are –2.0% and –7.9%, respectively. The compressive strength loss rates of the S-M5F and O-M5F specimens in the control group are –11.2% and –10.5%, respectively, while the flexural strength loss rates are –10.7 and –10.6%.

In the second stage, the strength transition period at 30 to 60 days, the secondary hydration of alkali-activated materials decreases.[26,27] The accumulation of sulfate erosion products reaches a certain degree, which weakens the strength growth of the specimen. Sulfate erosion products

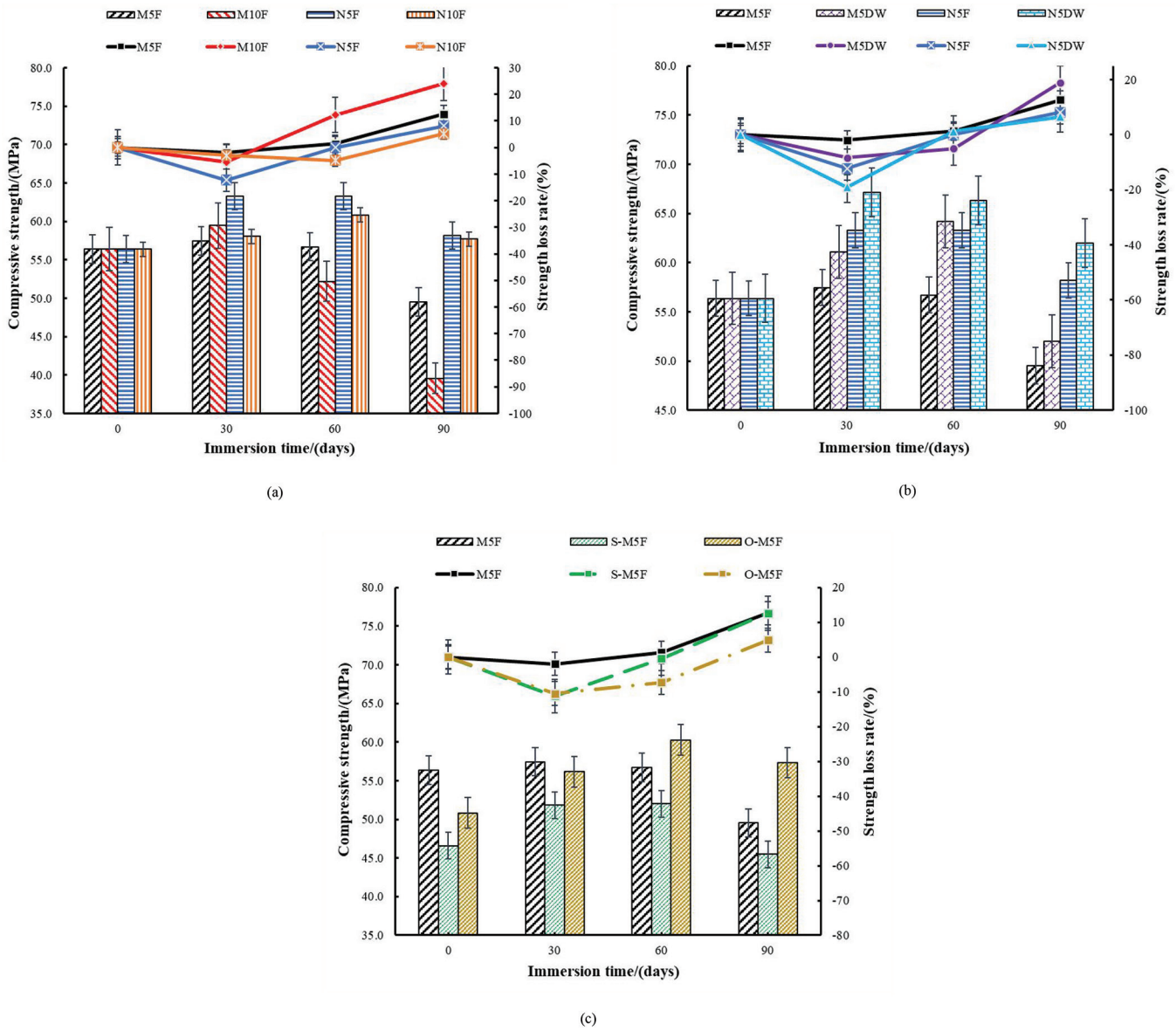

Fig. 3—(a) Effect of different sulfate concentrations on compressive strength; (b) effect of different erosion methods on compressive strength; and (c) effect of control group on compressive strength at different erosion times.

accumulate continuously, adhere to the inner walls of the pores, fill the pores, and increase pore wall pressure.[28] In addition to increasing pore pressure, it also effectively hinders the corrosion progress of the sulfate solution. At this stage, the compactness of the specimen increases, while the pore structure decreases. Figures 3 and 4 reveal that the N5DW and M10F specimens present the greatest degree of strength variation in the transition phase, which is consistent with the first stage. The compressive and flexural strength loss rates for N5DW increase from –19.1 and –2.2% to 1.2 and 6.2%, while the loss rates for M10F increase from –5.5 and –13.5% to 12.3 and 16.2%. In contrast to the strength change of each specimen in the control group, the strength of the M5F and S-M5F specimens in the alkali-activated group complete the transition from growth to loss. However, the strength of the O-M5F specimens still grows steadily, and the compressive and flexural strength loss rates change from –10.5 and –10.6% to –7.3 and –4.6%. These results display some similarities with the findings of Ganjian and Pouya.[29]

In the final 30 days, the decreasing strength stage, the erosion products in the pores of the specimens accumulate continuously, and the expansion stress of the pore walls increases continuously. At the same time, microcracks appear and develop, leading to a rapid decrease in the strength of the specimen. Under certain conditions, the activity of the slag and fly ash is slightly lower than cement and is characterized by early strength and rapid hardening. It is easy for relatively large pores to form between the mortars of the specimens, resulting in a weakening of the bonding force. Therefore, the compressive strength increases rapidly in the early stages, while corrosion damage is more obvious in the later stages. By observing the strength change of each specimen in Fig. 3 and 4, it can be observed that the strength loss of the M10F and M5DW specimens are the largest. The loss rates of compressive strength are 24.1 and 19.0%, while the loss rates of flexural strength are 6.3 and 2.4%. In the control group, the strength of the O-M5F samples did not change significantly, with a loss in compressive strength

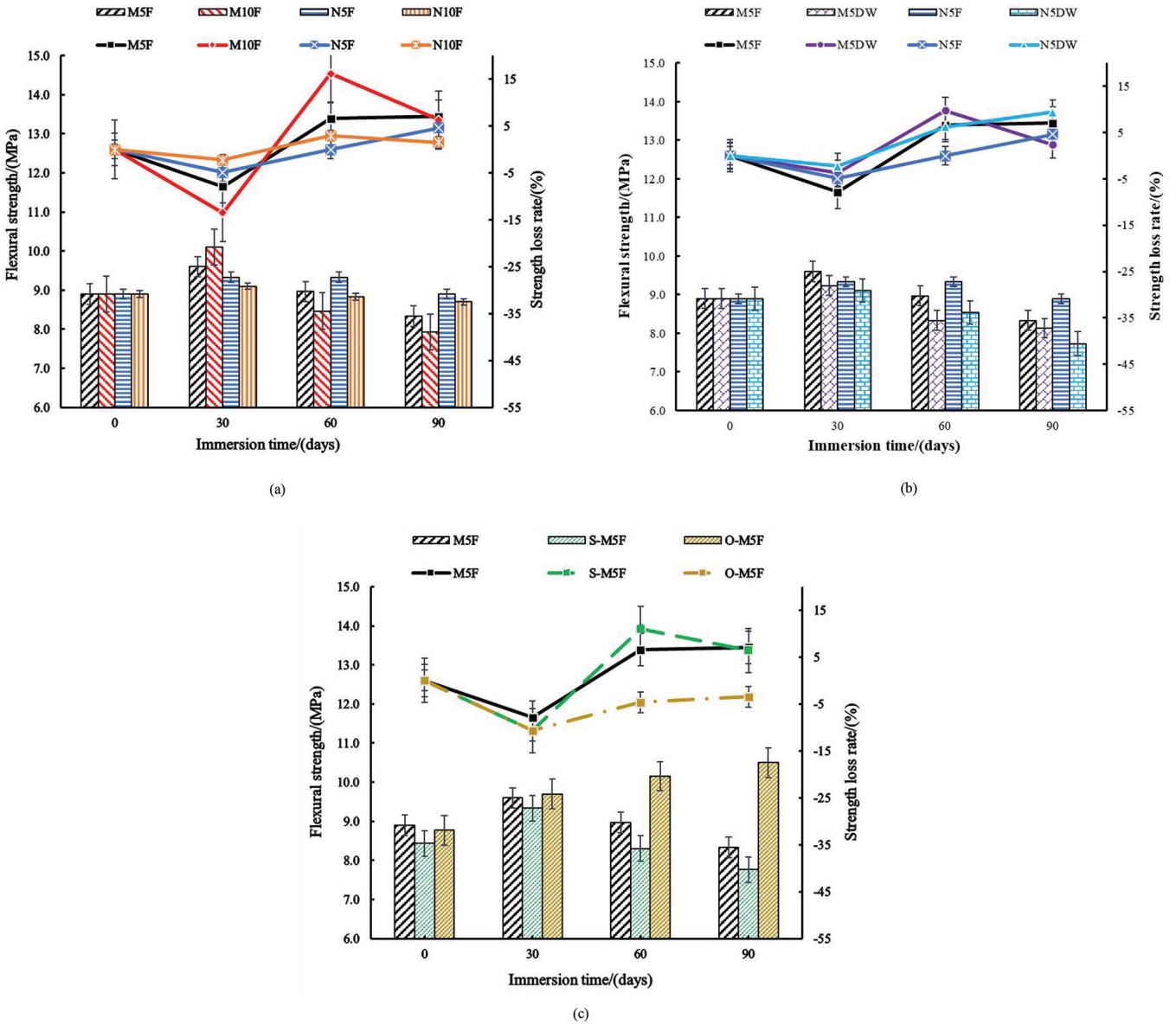

Fig. 4—(a) Effect of different sulfate concentrations on flexural strength; (b) effect of different erosion methods on flexural strength; and (c) effect of control group on flexural strength at different erosion times.

from –7.3 to –4.6% and a loss of flexural strength between 4.9 and –3.4%. The compressive and flexural strengths of M5F and S-M5F continued to decrease, with 12.6 and 12.6% losses in compressive strength, and 7.1 and 6.4% losses in flexural strength.

In summary, from the perspective of sulfate species, concentration, and erosion mode, the erosion of $MgSO_4$ is significantly greater than Na_2SO_4. Besides, high-concentration sulfate experiences greater erosion than low-concentration sulfate, and the erosion mode of the sulfate wetting-and-drying cycle is greater than full immersion. Concerning the sulfate erosion resistance of the three materials, after 90 days of erosion, the sulfate-resistance ability of the mechanically ground alkali-activated cementitious material is stronger than the sample prepared by simple mixing but is still less resistant than OPC. In contrast to the experimental findings of this study, Karakoç et al.[30] and Alcamand et al.[31] concluded that although the strength of alkali-excited materials decreases with increasing sulfate concentration and erosion time in the early stages of erosion, the strength decreases to a lesser extent in the later stages of erosion.

Analysis of erosion products and erosion mechanism

Fourier-transform infrared spectroscopy—To reduce the error of the test results, a fragment 5 mm away from the surface of the mortar specimens was chosen as the microscopic test sample. Figure 5 presents the schematic diagram of the experiment. Based on the change rule of chemical composition and functional groups of erosion products, the influence mechanism of sulfate type, sulfate concentration, and erosion mode on sulfate erosion of the mortar specimens was explored. Figures 6 to 8 display the FTIR curves of the specimens under different erosion conditions.

Existing research[32-34] shows that according to different sulfate erosion products, sulfate erosion types are divided into the following three types: ettringite ($3CaO{\cdot}Al_2O_3{\cdot}3CaSO_4{\cdot}32H_2O$), gypsum ($CaSO_4$), and thaumasite

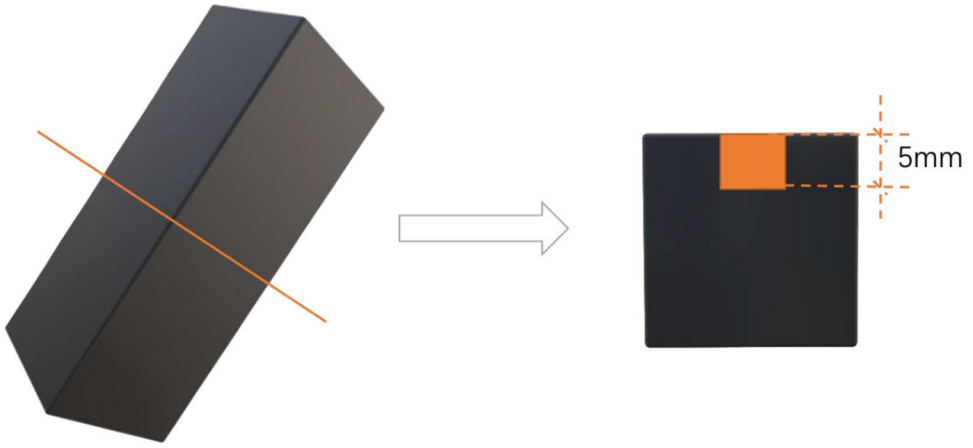

Fig. 5—Diagram of test sample sampling.

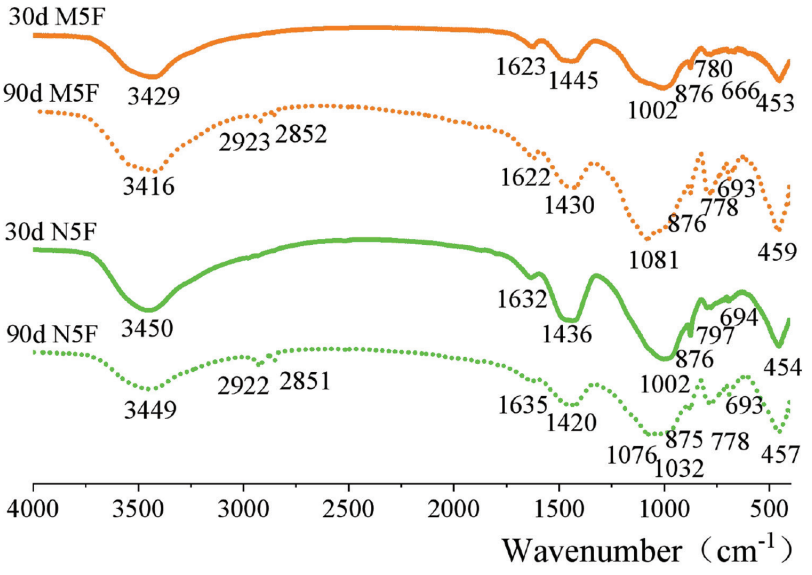

(a)

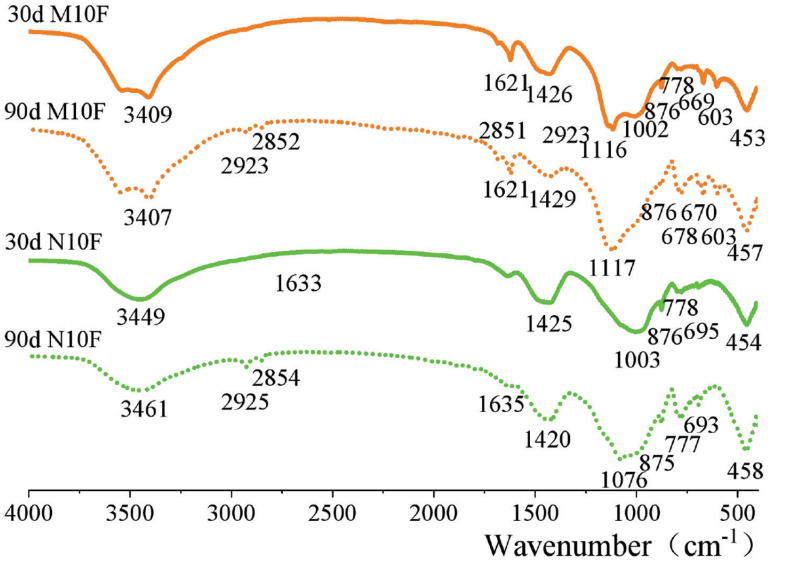

(b)

Fig. 6—(a) FTIR spectra at 5% erosion concentration; and (b) FTIR spectra at 10% erosion concentration.

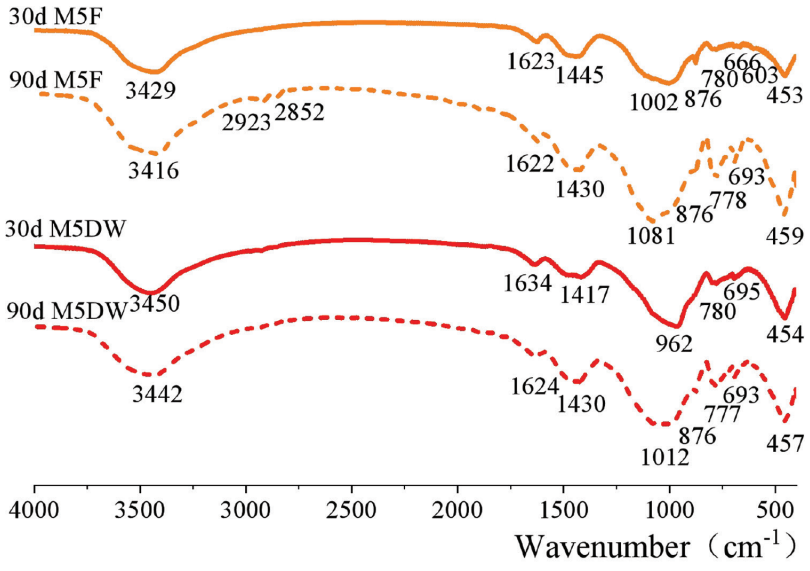

(a)

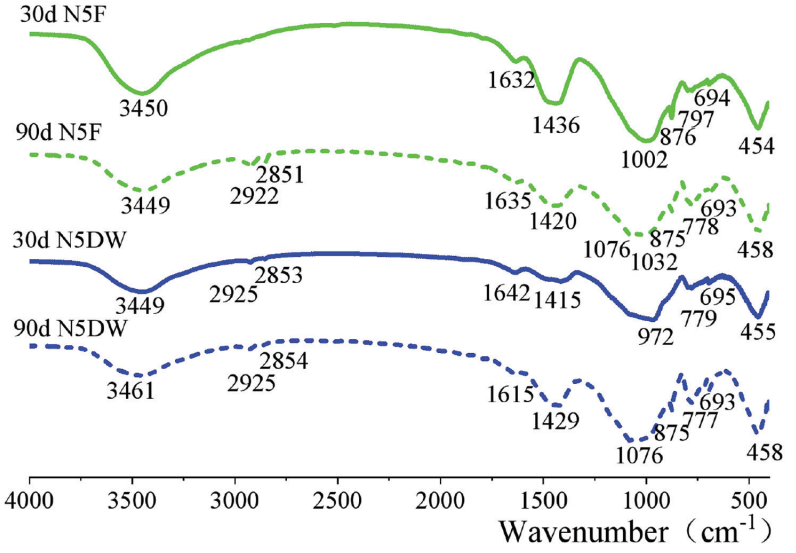

(b)

Fig. 7—(a) FTIR spectra of $MgSO_4$ solution under erosion conditions; and (b) FTIR spectra of Na_2SO_4 solution under erosion conditions.

($CaCO_3 \cdot CaSiO_3 \cdot CaSO_4 \cdot 15H_2O$). According to the FTIR curves in Fig. 6 to 8, the stretching vibration of the S-O bond at 1080 cm^{-1} and the bending vibration peak at 603 cm^{-1} appear, indicating that SO_4^{2-} exists in the sample. The characteristic peaks at 660 and 460 cm^{-1} indicate that gypsum crystals also exist in the sample,[35] but the stretching vibration characteristic peaks of the Al-O bond and SiO_6 are not observed at 550 and 750 cm^{-1}. Therefore, it can be preliminarily speculated that the mechanochemical one-part alkali-activated material mostly experiences gypsum-type erosion damage under sulfate attack. Additionally, there are obvious characteristic peaks at 876 and 1458 cm^{-1} bands in the sulfate attack specimens. These are caused by bending vibration and stretching vibration of the O-C-O bond,[36] indicating that carbonate is present in the sample. With the erosion of sulfate into the interior of the specimen, the content of metal cations (Mg^{2+} and Na^+) in the pore solution of the specimen increases significantly. There is a certain concentration of OH^- in the pore solution, so Mg^{2+} and OH^- can easily combine to form $Mg(OH)_2$ with lower solubility, as Eq. (1) shows. This subsequently leads to aggregation of the O-H bond, which is confirmed by the characteristic peaks of O-H bonds causing stretching and bending vibrations in the 3410 and 1620 cm^{-1} bands.[37]

$$Ca(OH)_2 + Mg^{2+} + SO_4^{2-} \rightarrow CaSO_4 + Mg(OH)_2 \quad (1)$$

$$C(\text{-A})\text{-S-H} + Mg^{2+} + SO_4^{2-} + 2H_2O \rightarrow M(\text{-A})\text{-S-H} + 2H_2O \cdot CaSO_4 \quad (2)$$

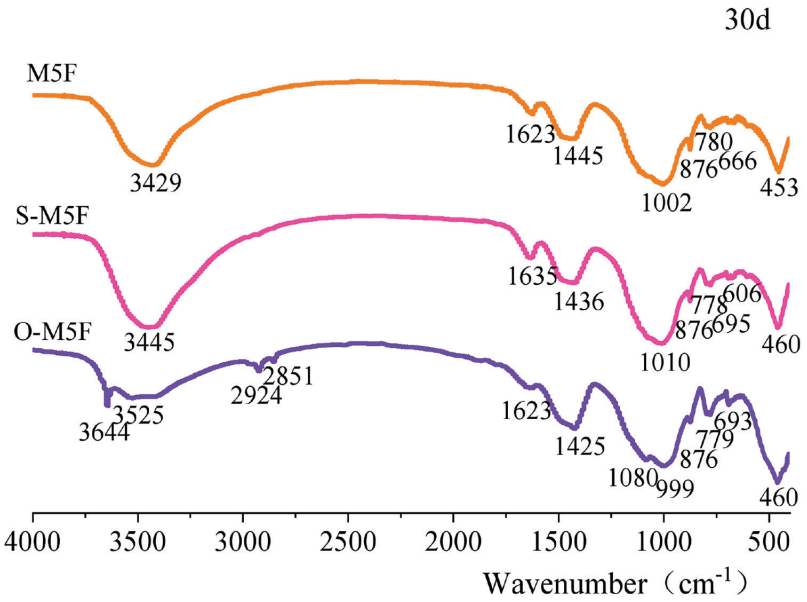

(a)

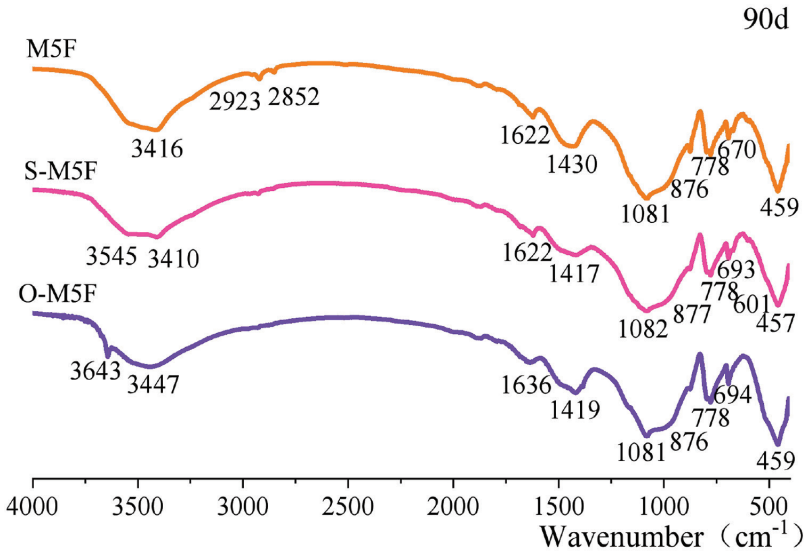

(b)

Fig. 8—(a) FTIR spectra of eroded 30-day specimens; and (b) FTIR spectra of eroded 90-day specimens.

Figure 6 presents the FTIR change of sulfate species and concentrations on the erosion products of mortar specimens. Compared with Na_2SO_4 erosion, under the action of $MgSO_4$ erosion, the FTIR curve has more characteristic peaks of gypsum at the 603 and 660 cm^{-1} bands. At the same concentration, the gypsum content after 90 days is higher than at 30. At the same stage, the characteristic peak of gypsum on M10F is more obvious than for M5F, indicating that the gypsum content increases with erosion time and concentration. With larger Mg^{2+} concentrations in the solution, Ca^{2+} is removed from C-S-H and C-A-S-H and Mg^{2+} replaces Ca^{2+} to form new M-S-H and M-A-S-H without bond strength.[38,39] Subsequently, the dissociated Ca^{2+} combines with SO_4^{2-} to form expansive gypsum, such as in Eq. (2). The volume of $2H_2O{\cdot}CaSO_4$ formed with pore water increases by a factor of 1.24. Besides, the pores of the specimens are subjected to expansion and extrusion pressure on the pore walls due to an increase in the volume of erosion products, resulting in the generation of microcracks. The width of the cracks grows with increased concentrations and erosion time, and the strength of the specimen also decreases rapidly. The phenomenon of specimen edges falling off also becomes more serious with increased concentrations. Figure 9(a) illustrates the appearance of the specimens. Characteristic peaks near 2925 cm^{-1} appear on the FTIR curve, revealing that calcite is produced by $MgSO_4$ and Na_2SO_4 solution erosion. The characteristic peaks of calcite produced by sodium salt are more obvious. Compared with $MgSO_4$ salt erosion, sodium salt erosion also has its unique erosion products. The characteristic peak intensities of the Na_2SO_4 erosion specimens at 876 cm^{-1} and 1458 cm^{-1} bands are more obvious, indicating that more carbonates are generated in the Na_2SO_4 erosion specimens. This carbonate does not result in excessive volume expansion, and the integrity of

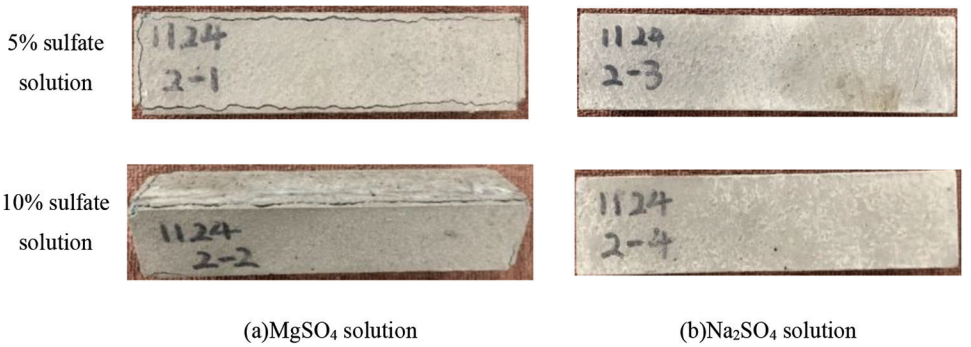

Fig. 9—Appearance effect of sulfate type and concentration on appearance of specimens after 90 days of corrosion.

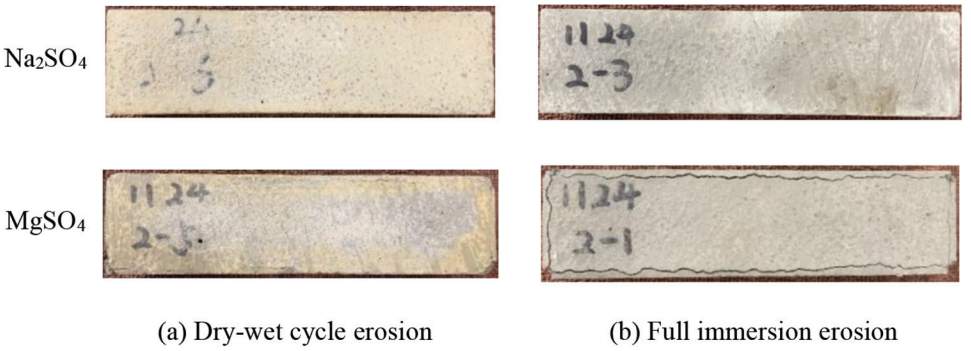

Fig. 10—Appearance effect of different erosion modes on specimens after 90 days of corrosion.

the specimen appears strong, without any obvious cracks, as Fig. 9(b) shows. This is consistent with the research results of Ismail et al.,[39] which stated that Na^+ ions are useful in maintaining the chemical stability of the pore solution of alkali-activated mortar specimens, while Mg^{2+} ions destroy C-S-H condensation.

Figure 7 represents FTIR changes of the erosion products of mortar specimens by sulfate erosion. Under $MgSO_4$ erosion, a weak characteristic peak at the 603 cm^{-1} band appears in the M5F specimen at 30 days, but a characteristic peak was not observed in the wetting-and-drying cycle erosion specimen. For specimens at the 90-day stage, characteristic peaks appear near 660 and 460 cm^{-1} in the two erosion modes. The characteristic peak of the specimen under full immersion is more obvious, indicating that gypsum is more likely to be produced by full-immersion erosion. Under the action of Na_2SO_4 solution erosion, the characteristic peak intensity of the N5DW specimen at 876 and 2925 cm^{-1} is greater than the N5F specimen, indicating that there is higher carbonate content in the wetting-and-drying cycle erosion specimen, which is in contact with the air for 8 hours when drying. The CO_2 in the air dissolves very easily in the surface adsorption water of the specimen. When the surface adsorption water gradually evaporates, it permeates the specimen through the liquid in the capillaries and promotes the carbonization of the specimen to produce calcium carbonate minerals. Observations indicate that the corners of the specimens subjected to wetting-and-drying cycle erosion appear to be detached, and their surfaces become rough and softened. For specimens subjected to full-immersion erosion, angular shedding is not obvious, but serious cracks occurred around the specimens corroded by $MgSO_4$ solution. Figure 10 shows the details.

Figure 8 presents the FTIR changes in erosion products of the one-part alkali-activated fly ash-slag mortar specimens prepared by the mechanochemical method, as well as the control group. Compared with O-M5F, the characteristic peak intensity of the S-M5F specimen at the 603 and 1100 cm^{-1} bands is more obvious, indicating that the gypsum content in the S-M5F specimen is higher. The stretching vibration frequency of O-H is in the range of 3550 to 3720 cm^{-1}, and the characteristic peak of 3644 cm^{-1} in the FTIR curve of the O-M5F corresponds to $Ca(OH)_2$. In contrast to the hydration products of traditional PC, the cohesive cementing of alkali-activated materials is mainly achieved by C-S-H and C-A-S-H. Thus, $Ca(OH)_2$ is not produced, which is consistent with the results of Komljenović et al.[40] The bond energy of C-O is lower than the C-S bond and is easier to break. Therefore, when $MgSO_4$ erodes, it preferentially reacts with $Ca(OH)_2$. The presence of $Ca(OH)_2$ effectively protects the stability of the C-S-H gel, while the alkali-activated material does not contain $Ca(OH)_2$. Compared to N-A-S-H, C-S-H and C-A-S-H are less resistant to sulfate,[41,42] causing a greater destructive effect. $MgSO_4$ erosion may destroy C-S-H and C-A-S-H gel, resulting in a more damaging effect. This is why the resistance of traditional PC to sulfate attack is better than the other two groups of alkali-activated materials, and the apparent compactness of traditional PC specimens is superior. The apparent compactness of the main part of the specimens prepared by mechanochemistry and simple mixing is satisfactory, but cracks appeared at the edge of the specimens, as Fig. 11 illustrates.

(a) Preparation of mechanochemical fly ash-slag

(b) Preparation of simple mixing fly ash-slag

(c) Preparation of Traditional Silicate Cement

Fig. 11—Appearance effect of control specimen after 90 days of 5% $MgSO_4$ solution erosion.

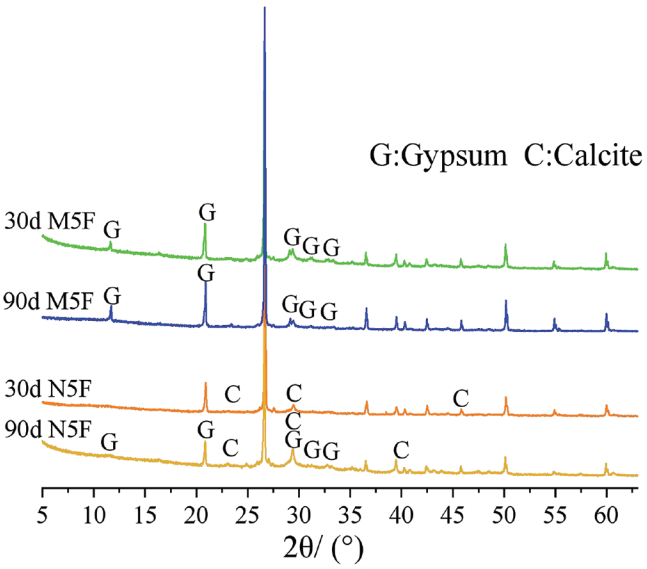

Fig. 12—XRD spectra of different sulfate attack specimens.

X-ray diffraction analysis—XRD is the most powerful method for studying inorganic crystal structures and is suitable for the phase analysis of crystalline materials. According to differences in the diffraction spectrum of the crystal in the number, angle position, relative intensity order, and shape of the diffraction peak, the constituent elements or groups of crystalline substances can be determined.

Figures 12 and 13 present XRD images of the sulfate attack specimens. For the XRD of mortar specimens, the diffraction peak intensity of quartz crystal at 25 to 28 degrees is extremely high, and this high diffraction peak masks the weak diffraction peaks of other crystals. At the positions of 25 to 30 degrees, a wide dispersion peak appears in the spectra, which indicates the existence of amorphous substances, mostly comprising N-A-S-H and C-A-S-H. Additionally, C-S-H gel causes the peaks at 32 to 40 degrees and 45 to 50 degrees.[43] In this study, the corrosion products of sulfate attack mortar specimens were analyzed using XRD analysis technology and compared with the results of the corrosion products obtained by FTIR analysis to obtain more accurate experimental results. According to the XRD analysis, the crystals in the erosion products mainly contain gypsum, $Ca(OH)_2$, and calcite.

Figure 12 displays XRD spectra of different sulfate attack specimens. The product of $MgSO_4$ solution erosion is mainly gypsum, while Na_2SO_4 solution erosion contains parts of gypsum, but mostly calcite. With increased erosion times from 30 to 90 days, the diffraction peak intensity of gypsum crystals in the XRD specimens increases moderately

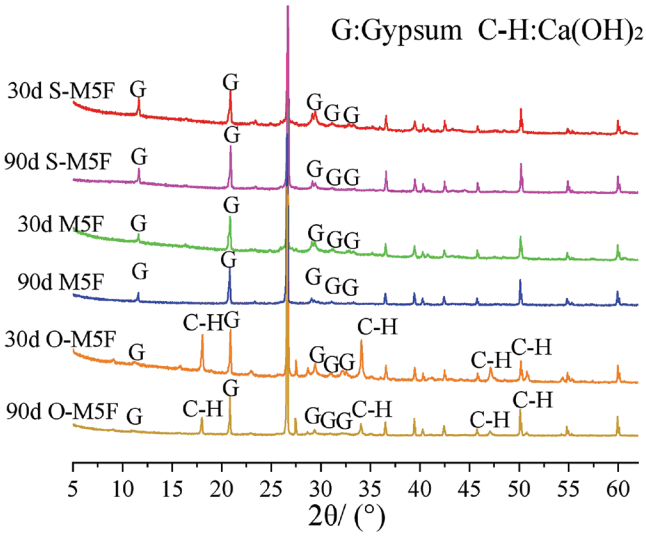

Fig. 13—XRD spectra of control immersion specimens.

for $MgSO_4$ solution erosion. However, the types of erosion products do not change. Comparing the erosion products of the Na_2SO_4 solution and the $MgSO_4$ solution, after 30 days, only the diffraction peak of calcite crystal was found in the XRD specimens of the Na_2SO_4 solution erosion products. At 90 days, there are many weak diffraction peaks of gypsum crystal in the XRD specimens, and the diffraction peak of calcite is also enhanced. This phenomenon further illustrates that $MgSO_4$ solution erosion produces a large amount of gypsum and results in severe gypsum-type erosion damage. For Na_2SO_4 solution erosion, in the early stage of erosion, the damage is mainly carbonized. However, in the later stage of erosion, carbonation degradation and gypsum erosion damage occur simultaneously. Nevertheless, sodium sulfate solution erosion produced less gypsum-type damage than magnesium sulfate solution erosion, which is consistent with the FTIR analysis results.

Figure 13 shows the XRD diagram of the immersed specimens from the control group. Compared with the one-part alkali-activated specimens prepared by mechanochemistry, the sulfate attack products all contain gypsum crystal diffraction peaks. When the erosion time is 30 days, the gypsum crystal diffraction peak intensity of the S-M5F specimen is greater than the M5F specimen, while the gypsum diffraction peak of the O-M5F specimen is not obvious. After 90 days, the diffraction peaks of gypsum in the control group were enhanced, indicating an increased accumulation of gypsum from erosion. Besides, the specimens exhibit expansion cracking, as Fig. 11 illustrates. In the XRD specimens, the O-M5F sample has an obvious $Ca(OH)_2$ diffraction peak, which is produced by the hydration of traditional silicate

cement. However, it could not be determined whether they are erosion products or not. In Fig. 13, the intensity of the $Ca(OH)_2$ diffraction peak of the O-M5F specimen decreases with longer invasion times. It is possible that the decrease in $Ca(OH)_2$ content is caused by resistance to sulfate attack. Sulfate invades the pore solution with high alkalinity, while Mg^{2+} and OH^- combine to form $Mg(OH)_2$. This substance is insoluble in water, and consequently reduces the alkalinity of the pore solution. To maintain the alkaline balance of the pore solution, the slightly soluble $Ca(OH)_2$ solid constantly dissolves in water, resulting in a continuous decrease of $Ca(OH)_2$ and causing a softening of colloidal sand and reduction in strength.[44] The hydration products of alkali-activated cementitious materials are mainly C-S-H and C-A-S-H, while almost no $Ca(OH)_2$ and stable bonded aluminum phases are produced.[45] Therefore, no $Ca(OH)_2$ diffraction peak was observed in the alkali-activated material specimens.

Mercury intrusion porosimetry—The pore structure connects the microstructure and macrostructure of the mortar, which is an important factor affecting mechanical properties and durability. There is a wide range of hole structure size distributions, the pore shape varies, and the system is complex. The pore structure may be divided into gel pores (<10 nm), transition pores (10 to 100 nm), capillary pores (100 to 1000 nm), and large pores (>1000 nm), according to the pore size.[46,47] Some scholars[48,49] believe that the strength and durability of concrete mainly depend on harmful pores larger than 100 nm, while pores smaller than 100 nm have a limited influence. In this section, MIP was used to analyze the porosity of mortar specimens against sulfate attack. This method measures pores with diameters of 0.005 to 1000 μm and provides valuable information regarding the pore structure analysis of concrete, as Fig. 14 displays.

Figure 14(a) shows the pore structure parameters of mortar specimens subjected to different types of sulfate attack. With increased erosion time, the pore structure distribution becomes homogenized, thus increasing the harmful pores and decreasing the porosity of the specimen. Taking $MgSO_4$ corrosion as an example, the porosity, gel pores, transition pores, capillary pores, and macropores of the 90-day specimens change by –24.55%, 11.75%, –49.80%, 18.61%, and 31.01%, respectively, compared with the 30-day specimens. For the $MgSO_4$ erosion specimens, in the early stage of erosion, new C-A-S-H and C-S-H gels are generated. This is due to the secondary volcanic ash reaction of fly ash, which may effectively fill the pores of specimens and increase the compactness. At the same time, the surplus gypsum produced by $MgSO_4$ erosion may fill the pores further. However, with an increase in the invasion time, the pozzolanic effect decreases, but the gypsum produced by erosion continues to increase. Excessive gypsum accumulation is certain to exert tremendous pressure on the pores, which increases the size of the small pores as well as the number of harmful pores. It also weakens erosion resistance and allows the large pores to progress into microfractures. When the microcracks connect, the specimen may suffer acute damage and the strength of the specimen may decrease rapidly. In the early stage of erosion of the Na_2SO_4 specimen, the calcium carbonate minerals produced by Na_2SO_4 erosion fill the pores and make them denser, thus enhancing the strength of the specimen. Furthermore, continuous accumulation of calcium carbonate minerals generates huge extrusion pressure on the pore walls, leading to microcracks inside the specimen and prompting a rapid reduction in strength. Therefore, a much more obvious reduction in strength occurs in the later stages of sulfate invasion.

Figure 14(b) illustrates the pore structure parameters of the control group mortar specimens. It was observed that the pore structure of O-M5F was not significantly different after 30 and 90 days of erosion, with harmless gel pores and transition pores accounting for 71.19% of the total pore structure at 30 days and 69.85% at 90 days. The main pore structures of S-M5F and M5F are also predominantly gel pores and transition pores, accounting for 71.53% and 61.91% of the total pore structure, respectively. Previous reports have shown that the pore size of alkali slag materials is mainly distributed between 1 and 20 nm, while the pore size of OPC is between 10 and 100 nm.[50,51] The O-M5F specimen has small porosity, and the C-S-H gel produced by conventional PC fills the pore structure and microcracks, leading to a reduction in the proportion of large pores and cracks with high compactness. This effectively prevents the sulfate erosion solution from entering the interior of the specimen and slows down the replacement reaction of Mg^{2+} and SO_4^{2-} with Ca^{2+} in C-S-H, thus reducing the damage caused by sulfate erosion.

The gel pore occupancy of the alkali-excited material is greater, and the water absorption rate is two to three times higher than OPC,[52,53] which provides Mg^{2+} and SO_4^{2-} with excellent channels for erosion, allowing them to gradually migrate to the interior of the specimen with the pore solution. Additionally, the concentration of alkali metal ions in the pore solution of the alkali slag material is high, exceeding OPC by nearly 10 times.[54] The high alkalinity of the pore solution provides suitable reaction conditions for Mg^{2+}, OH^-, and SO_4^{2-} to combine with Ca^{2+} in C(-A)-S-H, destroying the C(-A)-S-H gel bonds and making the pore structure of the specimen flimsy. However, the flimsy pore structure further contributes to the accelerated erosion rate, and the alkali-excited material specimens suffer severe erosion damage. Mechanical-force chemistry not only further activates the volcanic ash activity of the precursors, but also allows the precursors and alkali excipients to mix sufficiently for a stable and effective volcanic ash reaction, resulting in higher strength, less porosity, and superior resistance to sulfate in M5F than in S-M5F.

CONCLUSIONS

In this paper, the mechanochemical preparation of one-part alkali-excited mortars for resistance to sulfate attack was systematically studied. Based on macro and micro experimental data and experimental results, the following conclusions were obtained:

1. The tests in this paper show that highly concentrated $MgSO_4$ solution damages the strength of the specimens most severely under wetting-and-drying cyclic conditions. This is probably because the $MgSO_4$ solution not only provides

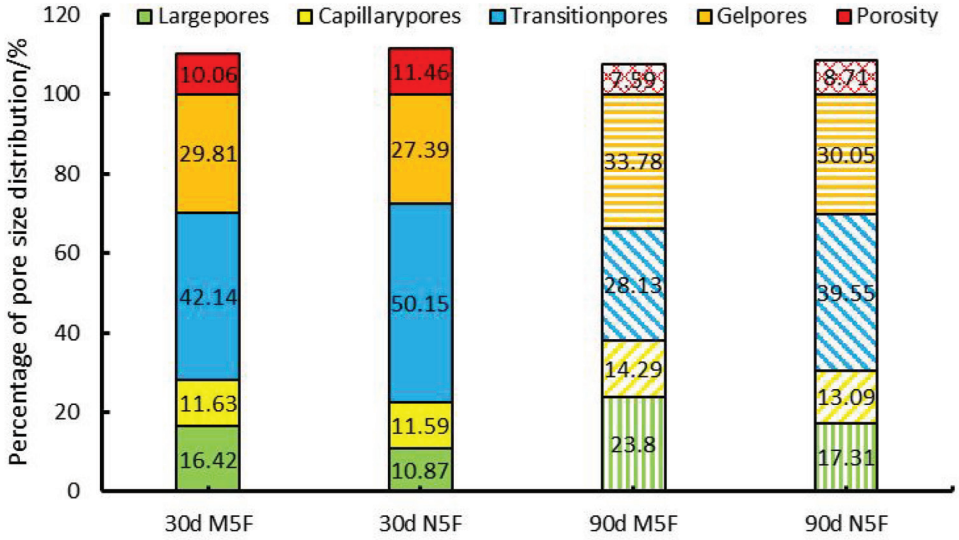

(a)

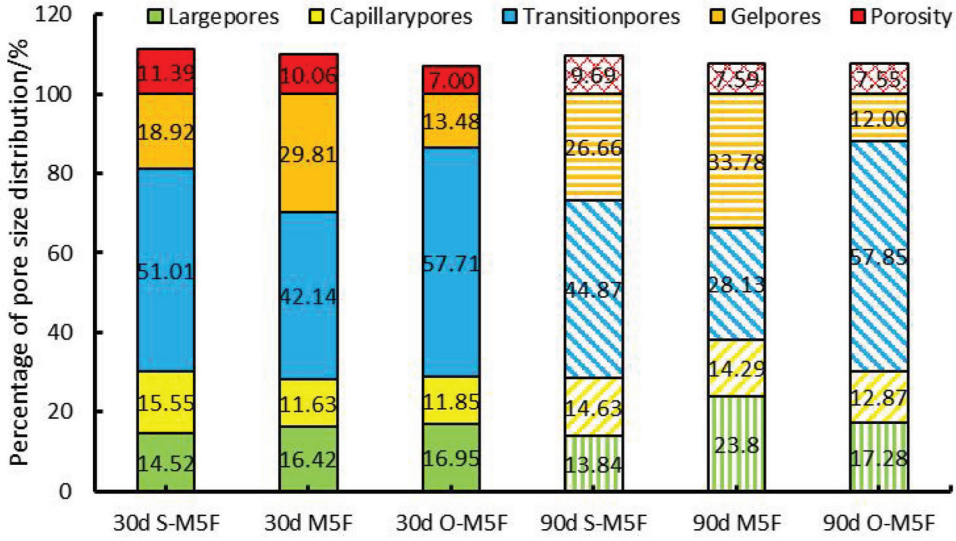

(b)

Fig. 14—(a) Pore structure changes under different kinds of sulfate erosion conditions; and (b) changes in pore structure of control group under different erosion time conditions.

erosive SO_4^{2-} ions, but Mg^{2+} ions are also involved in the erosion process. Moreover, there are variations in the sensitivity of flexural and compressive strength to different types of sulfate erosion. The compressive strength of specimens is more sensitive to $MgSO_4$ solution erosion, and the flexural strength is more sensitive to Na_2SO_4 solution erosion.

2. The mechanical-force chemical activation of gelling material precursors promotes the fine release of precursor particles with the promotion of volcanic ash activity and allows full mixing of the precursors and solid alkali-excitation agent. The adequate mixing of single-part alkali-excited materials provides a guarantee for stable and effective volcanic ash reactions. This is reflected in both porosity and strength, because M5F has lower porosity than S-M5F, while M5F has higher strength than S-M5F.

3. Under different types of sulfate erosion, the erosion products vary. According to Fourier-transform infrared spectroscopy (FTIR) and X-ray diffraction (XRD) analysis, it was observed that under Na_2SO_4 solution erosion, the erosion products of the specimen are mainly calcite in the early stage and a combination of calcite and gypsum in the later stage. For $MgSO_4$ solution erosion, the erosion products generated inside the specimen are gypsum, which indicates gypsum-type swelling erosion damage.

4. The mechanism of resistance to sulfate attack varies between alkali-stimulated cementitious materials and ordinary portland cement (OPC). The Ca^{2+} in C-A-S-H in alkali-excited cementitious materials is replaced by Na^+ and Mg^{2+} ions, and free Ca^{2+} combines with SO_4^{2-} to produce gypsum. Conventional silicate cements contain large amounts of $Ca(OH)_2$, which provides Ca^{2+} and slows the rate of C-S-H gel destruction, resulting in silicate cement samples that maintain some steady-state strength loss and pore structure

damage at 90 days of erosion, with less damage than alkali-excited specimens.

5. In this paper, the three aspects of sulfate type, concentration, and erosion mode were studied to simulate a genuine erosion environment. However, real environments are very complex and factors such as load size, temperature change, and sulfate type all have an impact on erosion. Therefore, further investigations are required to understand the mechanism of sulfate erosion from other aspects, which will help to improve the study of the sulfate erosion of alkali-excited materials.

AUTHOR BIOS

Wenda Wu *is an Associate Researcher, Master Supervisor, and Quanzhou Talent Harbor High-Level Talent in Quanzhou, Fujian, China. He attended the School of Advanced Manufacturing at Fuzhou University, Fuzhou, Fujian, China. His research interests include alkali-excited cements/concrete, self-consolidating concrete materials/structural properties, and recycled concrete materials/structural properties.*

Shilong Ma *is a Graduate Student in the School of Advanced Manufacturing at Fuzhou University. His research interests include one-part alkali-excited materials.*

Yuanda Wang *is a Graduate Student in the College of Civil Engineering at Fuzhou University. His research interests include the durability performance of alkali-excited materials.*

Xuefang Wang *is an Associate Researcher and Master Supervisor in Fujian, China. She received her PhD in engineering from the School of Advanced Manufacturing at Fuzhou University. Her research interests include the research and application of self-consolidating high-performance concrete and its structure, research on volume stability and durability of high-performance concrete and its ratio optimization design, and environmentally friendly and energy-saving cement-based materials.*

Liwei Xu *is a Professor, Senior Engineer, Master's Degree Supervisor, and was a Visiting Scholar at Michigan State University, East Lansing, MI, in 2016, and at the University of Applied Sciences, Cologne, Germany, in 2011.*

Shichang Ye *is an Engineer at Sanming Yiyuan Electric Power Survey and Design Co., Ltd.*

ACKNOWLEDGMENTS

The authors would like to thank the China Postdoctoral Science Foundation for providing equipment and funding for this work. This work was supported by the National Outstanding Youth Science Fund Project of the National Natural Science Foundation of China (Grant No. 51808124), the Innovative Research Group Project of the National Natural Science Foundation of China (Grant No. 2019M652246), and the Fujian Provincial Department of Science and Technology (Grant No. 2019HZ07011). The authors declare that they have no known competing financial interests or personal relationships that might affect the work reported in this paper.

REFERENCES

1. Shi, C; Krivenko, P. V.; and Roy, D., *Alkali-Activated Cements and Concretes*, Taylor & Francis, London, UK, 2006.

2. Pacheco-Torgal, F.; Castro-Gomes, J.; and Jalali, S., "Alkali-Activated Binders: A Review: Part 1. Historical Background, Terminology, Reaction Mechanisms and Hydration Products," *Construction and Building Materials*, V. 22, No. 7, 2008, pp. 1305-1314. doi: 10.1016/j.conbuildmat.2007.10.015

3. Purdon, A. O., "The Action of Alkalis On Blast-Furnace Slag," *Journal of the Society of Chemical Industry*, V. 59, No. 9, 1940, pp. 191-202.

4. Duxson, P., and Provis, J. L., "Designing Precursors for Geopolymer Cements," *Journal of the American Ceramic Society,* V. 91, No. 12, 2008, pp. 3864-3869. doi:10.1111/j.1551-2916.2008.02787.x

5. Peng, M. X.; Wang, Z. H.; Shen, S. H.; Xiao, Q. G.; Li, L. J.; Tang, Y. C.; and Hu, L. L., "Alkali Fusion of Bentonite to Synthesize One-Part Geopolymeric Cements Cured at Elevated Temperature by Comparison With Two-Part Ones," *Construction and Building Materials*, V. 130, 2017, pp. 103-112 doi: 10.1016/j.conbuildmat.2016.11.010

6. Habert, G.; d'Espinose de Lacaillerie, J. B.; and Roussel, N., "An Environmental Evaluation of Geopolymer Based Concrete Production: Reviewing Current Research Trends," *Journal of Cleaner Production,* V. 19, No. 11, 2011, pp. 1229-1238. doi: 10.1016/j.jclepro.2011.03.012

7. McLellan, B. C.; Williams, R. P.; Lay, J.; van Riessen, A.; and Corder, G. D., "Costs and Carbon Emissions For Geopolymer Pastes in Comparison to Ordinary Portland Cement," *Journal of Cleaner Production*, V. 19, No. 9-10, 2011, pp. 1080-1090. doi: 10.1016/j.jclepro.2011.02.010

8. Davidovits, J.; Comrie, D. C.; Paterson, J. H.; and Ritcey, D. J., "Geopolymeric Concretes for Environmental Protection," *Concrete International*, V. 12, No. 7, July 1990, pp. 30-40.

9. Stellacci, P.; Liberti, L.; Notarnicola, M.; and Bishop, P. L., "Valorization of Coal Fly Ash by Mechano-Chemical Activation: Part I. Enhancing Adsorption Capacity," *Chemical Engineering Journal,* V. 149 No. 1-3, 2009, pp. 11-18. doi: 10.1016/j.cej.2008.06.043

10. Temuujin, J.; Williams, R. P.; and van Riessen, A., "Effect of Mechanical Activation of Fly Ash on the Properties of Geopolymer Cured at Ambient Temperature," *Journal of Materials Processing Technology,* V. 209, No. 12-13, 2009, pp. 5276-5280. doi: 10.1016/j.jmatprotec.2009.03.016.10.1016

11. Kumar, R.; Kumar, S.; Badjena, S.; and Mehrotra, S. P., "Hydration of Mechanically Activated Granulated Blast Furnace Slag," *Metallurgical and Materials Transactions B*, V. 36, No. 6, 2005, pp. 873-883. doi: 10.1007/s11663-005-0089-x

12. Zhao, J.; Wang, D.; and Liao, S., "Effect of Mechanical Grinding on Physical and Chemical Characteristics of Circulating Fluidized Bed Fly Ash From Coal Gangue Power Plant," *Construction and Building Materials*, V. 101, Part 1, 2015, pp. 851-860. doi: 10.1016/j.conbuildmat.2015.10.144

13. Feng, P.; Garboczi, E. J.; Miao, C.; and Bullard, J. W., "Microstructural Origins of Cement Paste Degradation by External Sulfate Attack," *Construction and Building Materials*, V. 96, 2015, pp. 391-403. doi: 10.1016/j.conbuildmat.2015.07.186

14. Ikumi, T.; Cavalaro, S. H. P.; Segura, I.; de la Fuente, A.; and Aguado, A., "Simplified Methodology to Evaluate the External Sulfate Attack in Concrete Structures," *Materials & Design*, V. 89, 2016, pp. 1147-1160. doi: 10.1016/j.matdes.2015.10.084

15. Torres, S. M.; Sharp, J. H.; Swamy, R. N.; Lynsdale, C. J.; and Huntley, S. A., "Long Term Durability of Portland-Limestone Cement Mortars Exposed to Magnesium Sulfate Attack," *Cement and Concrete Composites*, V. 25, No. 8, 2003, pp. 947-954. doi: 10.1016/S0958-9465(03)00160-4

16. Lothenbach, B.; Bary, B.; Le Bescop, P.; Schmidt, T.; and Leterrier, N., "Sulfate Ingress in Portland Cement," *Cement and Concrete Research*, V. 40, No. 8, 2010, pp. 1211-1225. doi: 10.1016/j.cemconres.2010.04.004

17. Al-Amoudi, O. S. B., "Attack on Plain and Blended Cements Exposed to Aggressive Sulfate Environments," *Cement and Concrete Composites*, V. 24, No. 3-4, 2002, pp. 305-316. doi: 10.1016/S0958-9465(01)00082-8

18. Comanescu, I.; Melchers, R.E.; and Taxén, C., "Corrosion and Durability of Offshore Steel Water Injection Pipelines," *Ships and Offshore Structures*, V. 11, No. 4, 2016, pp. 424-437. doi: 10.1080/17445302.2015.1014249

19. Rabeh, M.; Petersen, J.; and O'Hearn, S., "Insulation Optimization Improves Safety, Reduces Corrosion Risks," *Offshore*, V. 78, No. 2, 2018, pp. 32-33. doi: 10.14359/51663865

20. Tan, L.; Wang, F.; Liang, M.; Wang, X.; Das, R.; Mao, D.; and Luo, Y., "Antibiotic Resistance Genes Attenuated With Salt Accumulation in Saline Soil," *Journal of Hazardous Materials*, V. 374, 2019, pp. 35-42. doi: 10.1016/j.jhazmat.2019.04.020

21. Wang, X.; Xue, Z.; Lu, X.; Liu, Y.; Liu, G.; and Wu, Z., "Salt Leaching of Heavy Coastal Saline Silty Soil by Controlling the Soil Matric Potential," *Soil and Water Research*, V. 14, No. 3, 2019, pp. 132-137. doi: 10.17221/106/2018-SWR

22. Rui, H.; Zheng, S.; Gan, V. J. L.; Wang, Z.; Fang, J.; and Shao, Y., "Damage Mechanism and Interfacial Transition Zone Characteristics of Concrete under Sulfate Erosion and Dry-Wet Cycles," *Construction and Building Materials*, V. 255, 2020, Article No. 119340. doi: 10.1016/j.conbuildmat.2020.119340

23. Cao, M. L.; Yao, H.; and Cui, S. C., "Experimental Study on Impact Resistance of $CaCO_3$ Whisker-Reinforced Cement Mortar," *Applied Mechanics and Materials*, V. 99-100, Sept. 2011, pp. 706-710. doi: 10.4028/www.scientific.net/AMM.99-100.706

24. Ikumi, T., and Segura, I., "Numerical Assessment of External Sulfate Attack in Concrete Structures. A Review," *Cement and Concrete Research*, V. 121, 2019, pp. 91-105. doi: 10.1016/j.cemconres. 2019.04.010

25. Sun, D.; Wu, K.; Shi, H.; Zhang, L.; and Zhang, L., "Effect of Interfacial Transition Zone on the Transport of Sulfate Ions in Concrete," *Construction and Building Materials*, V. 192, Dec. 2018, pp. 28-37 doi: 10.1016/j.conbuildmat. 2018.10.140

26. Kong, L.; Ge, Y.; Zhang, B.; and Zhang, W., "Effect of Water Release of Lightweight Aggregate on Secondary Hydration of Fly Ash," *Kuei*

Suan Jen Hsueh Pao/Journal of the Chinese Ceramic Society, V. 37, 2009, pp. 1239-1243.

27. Quan, X.; Wang, S.; Liu, K.; Zhao, N.; Xu, J.; Xu, F.; and Zhou, J., "The Corrosion Resistance of Engineered Cementitious Composite (ECC) Containing High-Volume Fly Ash and Low-Volume Bentonite against the Combined Action of Sulfate Attack and Dry-Wet Cycles," *Construction and Building Materials*, V. 303, No. 11, Oct. 2021, Article No. 124599

28. Wang, K.; Guo, J.; Liu, X.; Yang, L.; and Zhang, P., "Effect of Dry–Wet Ratio on Pore-Structure Characteristics of Fly Ash Concrete under Sulfate Attack," *Materials and Structures*, V. 54, No. 3, 2021, Article No. 100. doi: 10.1617/s11527-021-01700-2

29. Ganjian, E., and Pouya, H. S., "The Effect of Persian Gulf Tidal Zone Exposure on Durability of Mixes Containing Silica Fume and Blast Furnace Slag," *Construction and Building Materials*, V. 23, No. 2, 2009, pp. 644-652. doi: 10.1016/j.conbuildmat.2008.02.009

30. Karakoç, M. B.; Türkmen, I.; Maraş, M. M.; Kantarci, F.; and Demirboğa, R., "Sulfate Resistance of Ferrochrome Slag Based Geopolymer Concrete," *Ceramics International*, V. 42, No. 1, Part B, 2016, pp. 1254-1260. doi: 10.1016/j.ceramint.2015.09.058

31. Alcamand, H. A.; Borges, P. H. R.; Silva, F. A.; and Trindade, A. C. C., "The Effect of Matrix Composition and Calcium Content on the Sulfate Durability of Metakaolin and Metakaolin/Slag Alkali-Activated Mortars," *Ceramics International*, V. 44, No. 5, 2018, pp. 5037-5044. doi: 10.1016/j.ceramint.2017.12.102

32. Rozière, E.; Loukili, A.; El Hachem, R.; and Grondin, F., "Durability of Concrete Exposed to Leaching and External Sulphate Attacks," *Cement and Concrete Research*, V. 39, No. 12, 2009, pp. 1188-1198. doi: 10.1016/j.cemconres.2009.07.021

33. Kunther, W.; Lothenbach, B.; and Scrivener, K. L., "On the Relevance of Volume Increase for the Length Changes of Mortar Bars in Sulfate Solutions," *Cement and Concrete Research*, V. 46, 2013, pp. 23-29. doi: 10.1016/j.cemconres.2013.01.002

34. Müllauer, W.; Beddoe, R. E.; and Heinz, D., "Sulfate Attack Expansion Mechanisms," *Cement and Concrete Research*, V. 52, 2013, pp. 208-215. doi: 10.1016/j.cemconres.2013.07.005

35. Chang, J.; Gu, Y.; and Ansari, W. S., "Mechanism of Blended Steel Slag Mortar With CO_2 Curing Exposed to Sulfate Attack," *Construction and Building Materials*, V. 251, 2020, Article No. 118880. doi: 10.1016/j.conbuildmat.2020.118880

36. Yusuf, M. O., "Performance of Slag Blended Alkaline Activated Palm Oil Fuel Ash Mortar in Sulfate Environments," *Construction and Building Materials*, V. 98, 2015, pp. 417-424. doi: 10.1016/j.conbuildmat.2015.07.012

37. Lecomte, I.; Henrist, C.; Liégeois M.; Maseri, F.; Rulmont, A.; and Cloots, R., "(Micro)-Structural Comparison between Geopolymers, Alkali-Activated Slag Cement and Portland Cement," *Journal of the European Ceramic Society*, V. 26, No. 16, 2005, pp. 3789-3797. doi: 10.1016/j.jeurceramsoc.2005.12.021

38. Aydın, S., and Baradan, B., "Sulfate Resistance of Alkali-Activated Slag and Portland Cement Based Reactive Powder Concrete," *Journal of Building Engineering*, V. 43, 2021, Article No. 103205. doi: 10.1016/j.jobe.2021.103205

39. Ismail, I.; Bernal, S. A.; Provis, J. L.; Hamdan, S.; and van Deventer, J. S. J., "Microstructural Changes in Alkali Activated Fly Ash/Slag Geopolymers with Sulfate Exposure," *Materials and Structures*, V. 46, No. 3, 2013, pp. 361-373. doi: 10.1617/s11527-012-9906-2

40. Komljenović, M.; Baščarević, Z.; Marjanović, N.; and Nikolić, V., "External Sulfate Attack on Alkali-Activated Slag," *Construction and Building Materials*, V. 49, 2013, pp. 31-39. doi: 10.1016/j.conbuildmat.2013.08.013

41. Thokchom, S.; Ghosh, P.; and Ghosh, S., "Performance of Fly Ash Based Geopolymer Mortars in Sulphate Solution," *Journal of Engineering Science and Technology Review*, V. 3, No. 1, 2010, pp. 36-40.

42. Duan, P.; Yan, C.; and Zhou, W., "Influence of Partial Replacement of Fly Ash by Metakaolin on Mechanical Properties and Microstructure of Fly Ash Geopolymer Paste Exposed to Sulfate Attack," *Ceramics International*, V. 42, No. 2, Part B, 2016, pp. 3504-3517. doi: 10.1016/j.ceramint.2015.10.154

43. Aboulayt, A.; Riahi, M.; Ouazzani Touhami, M.; Hannache, H.; Gomina, M.; and Moussa, R., "Properties of Metakaolin Based Geopolymer Incorporating Calcium Carbonate," *Advanced Powder Technology*, V. 28, No. 9, 2017, pp. 2393-2401. doi: 10.1016/j.apt.2017.06.022

44. Chen, J.-K.; Qian, C.; and Song, H., "A New Chemo-Mechanical Model of Damage in Concrete under Sulfate Attack," *Construction and Building Materials*, V. 115, 2016, pp. 536-543. doi: 10.1016/j.conbuildmat.2016.04.074

45. Myers, R. J.; Bernal, S. A.; Gehman, J. D.; van Deventer, J. S. J.; and Provis, J. L., "The Role of Al in Cross-Linking of Alkali-Activated Slag Cements," *Journal of the American Ceramic Society*, V. 98, No. 3, 2015, pp. 996-1004. doi: 10.1111/jace.13360

46. Ozturk, A. U., and Baradan, B., "A Comparison Study of Porosity and Compressive Strength Mathematical Models with Image Analysis," *Computational Materials Science*, V. 43, No. 4, 2008, pp. 974-979. doi: 10.1016/j.commatsci.2008.02.011

47. Olsen, R. A.; Neubauer, C. M.; and Jennings, H. M., "Damage to the Pore Structure of Hardened Portland Cement Paste by Mercury Intrusion," *Journal of the American Ceramic Society*, V 80, No. 9, 1997, pp. 2454-2458. doi: 10.1111/j.1151-2916.1997.tb03144.x

48. Mehta, P. K., and Monteiro, P. J. M., *Concrete: Microstructure, Properties, and Materials*, McGraw-Hill, New York, 2006.

49. Jin, S.; Zhang, J.; and Han, S., "Fractal Analysis of Relation between Strength and Pore Structure of Hardened Mortar," *Construction and Building Materials*, V. 135, 2017, pp. 1-7. doi: 10.1016/j.conbuildmat.2016.12.152

50. Babaee, M., and Castel, A., "Water Vapor Sorption Isotherms, Pore Structure, and Moisture Transport Characteristics of Alkali-Activated and Portland Cement-Based Binders," *Cement and Concrete Research*, V. 113, 2018, pp. 99-120. doi: 10.1016/j.cemconres.2018.07.006

51. Li, Q.; Yang, Y.; Yang, K.; Chao, Z.; Tang, D.; Tian, Y.; Wu, F.; Basheer, M.; and Yang, C., "The Role of Calcium Stearate on Regulating Activation to Form Stable, Uniform and Flawless Reaction Products in Alkali-Activated Slag Cement," *Cement and Concrete Composites*, V. 103, 2019, pp. 242-251. doi: 10.1016/j.cemconcomp.2019.05.009

52. Li, Q.; Yang, K.; and Yang, C., "An Alternative Admixture to Reduce Sorptivity of Alkali-Activated Slag Cement by Optimising Pore Structure and Introducing Hydrophobic Film," *Cement and Concrete Composites*, V. 95, 2019, pp. 183-192. doi: 10.1016/j.cemconcomp.2018.11.004

53. Yang, K.; Yang, C.; Magee, B.; Nanukuttan, S.; and Ye, J., "Establishment of a Preconditioning Regime for Air Permeability and Sorptivity of Alkali-Activated Slag Concrete," *Cement and Concrete Composites*, V. 73, 2016, pp. 19-28. doi: 10.1016/j.cemconcomp.2016.06.019

54. Puertas, F.; Fernández-Jiménez, A.; Blanco-Varela, M. T., "Pore Solution in Alkali-Activated Slag Cement Pastes. Relation to the Composition and Structure of Calcium Silicate Hydrate," *Cement and Concrete Research*, V. 34, No. 1, 2004, pp. 139-148. doi: 10.1016/S0008-8846(03)00254-0